RESEARCH ARTICLE

National Science Review
10: nwad226, 2023
https://doi.org/10.1093/nsr/nwad226
Advance access publication 2 September 2023

MATERIALS SCIENCE

Green synthesis of bifunctional phthalocyanine-porphyrin COFs in water for efficient electrocatalytic CO_2 reduction coupled with methanol oxidation

Mi Zhang†, Jia-Peng Liao†, Run-Han Li†, Sheng-Nan Sun, Meng Lu, Long-Zhang Dong, Pei Huang, Shun-Li Li, Yue-Peng Cai and Ya-Qian Lan*

ABSTRACT

Electrocatalytic CO_2 reduction (ECR) coupled with organic oxidation is a promising strategy to produce high value-added chemicals and improve energy efficiency. However, achieving the efficient redox coupling reaction is still challenging due to the lack of suitable electrocatalysts. Herein, we designed two bifunctional polyimides-linked covalent organic frameworks (PI-COFs) through assembling phthalocyanine (Pc) and porphyrin (Por) by non-toxic hydrothermal methods in pure water to realize the above catalytic reactions. Due to the high conductivity and well-defined active sites with different chemical environments, NiPc-NiPor COF performs efficient ECR coupled with methanol oxidation reaction (MOR) (Faradaic efficiency of CO (FE_{CO}) = 98.12%, partial current densities of CO (j_{CO}) = 6.14 mA cm^{-2} for ECR, FE_{HCOOH} = 93.75%, j_{HCOOH} = 5.81 mA cm^{-2} for MOR at low cell voltage (2.1 V) and remarkable long-term stability). Furthermore, experimental evidences and density functional theory (DFT) calculations demonstrate that the ECR process mainly conducts on NiPc unit with the assistance of NiPor, meanwhile, the MOR prefers NiPor conjugating with NiPc. The two units of NiPc-NiPor COF collaboratively promote the coupled oxidation-reduction reaction. For the first time, this work achieves the rational design of bifunctional COFs for coupled heterogeneous catalysis, which opens a new area for crystalline material catalysts.

Keywords: hydrothermal synthesis, phthalocyanine-porphyrin COFs, bifunctional electrocatalysts, electrocatalytic CO_2 reduction, methanol oxidation reaction

INTRODUCTION

The massive consumption of fossil fuels all over the world has led to excessive CO_2 emissions into the atmosphere, which has caused serious environmental issues and energy crises [1–3]. Electrochemical CO_2 reduction (ECR) by renewable electric energy offers a promising strategy to convert CO_2 into useful energy substances, such as CO, CH_3OH, HCOOH, CH_4 and C_2H_4 *et al.*, which will simultaneously reduce CO_2 and produce useful energy fuels [4–8]. In recent years, multifarious ECR catalysts have been developed for CO_2 reduction, and high efficiencies have also been achieved, which showed great future prospects for practical uses. However, most studies only focused on the ECR half reaction at the cathode when evaluating catalytic performance, while neglecting the relevant oxidation half reaction on the anode side, thus causing a great waste of energy [9,10]. In most of the reported researches, the conventional method to treat anode reaction has been coupled with the water oxidation reaction (oxygen evolution reaction, OER) by using a carbon or platinum rod as the anode [11,12]. Unfortunately, this OER process will cause overpotential and also needs a high energy input due to slow kinetics and unfavorable thermodynamics of H_2O oxidation reaction, thus leading to lower energy efficiency for the overall catalytic reaction. Besides, the O_2 produced is relatively less value-added compared to many industrial chemicals [13,14]. Therefore, there is an urgent need to develop an oxidation reaction with high energy efficiency to replace the OER process.

The application of the anodic oxidation process to the organic molecules oxidative synthesis, such

School of Chemistry, South China Normal University, Guangzhou 510006, China

***Corresponding author.** E-mail: yqlan@m.scnu.edu.cn

†Equally contributed to this work.

Received 21 April 2023; **Revised** 15 June 2023; **Accepted** 17 August 2023

as methanol oxidation reaction (MOR) to produce HCOOH, can effectively improve energy efficiency due to low theoretical overpotential and also be in line with the demand of green chemistry [15–17]. However, it remains a challenge to enable these two electrocatalytic reactions to cooperate effectively. The main barrier in this field is the lack of highly active multifunctional electrocatalysts to fulfill these two processes. Theoretically, the electrocatalysts for ECR coupled with MOR should satisfy the following requirements: (1) highly active and accessible catalytic sites for reduction or oxidation reaction [18]; (2) affinity and adsorption activation for substrates such as CO_2 or methanol [19]; (3) preferable electron and proton transfer ability [20]; (4) high stability during the electrochemical measurements [21]. Until now, many researches have explored the activity of a single functional homogeneous catalyst (such as metal complex) for ECR or MOR separately, while the problems of recycling and stability are still difficult to solve [22,23]. The construction of bifunctional heterogeneous catalysts can effectively solve the above problems which is used for ECR coupled with MOR, yet this has rarely been studied. Among them, the well-defined model with precise structure is particularly important for studying the structure-function relationship and mechanism of bifunctional heterogeneous catalysts.

Covalent organic frameworks (COFs) with excellent structural designability and high stabilities are promising platforms for catalytic reactions [24–27]. Some building blocks of COFs possess appropriate coordination sites, thus making them capable of introducing metal active sites for typical catalysis [28,29]. Up to the present, COFs-based catalysts have been successfully applied for ECR, OER and oxygen reduction reaction (ORR), *et al.*, which illustrates the great potential for electrocatalysis [30,31]. However, the precise introduction of multiple active sites with different chemical environments into COFs is still in its infancy, much less their application in electrocatalysis. Recently, metallophthalocyanine (MPc) and metalloporphyrin (MPor) based-COFs have been studied for catalytic reactions [32,33]. Nevertheless, most of these works only focused on studying the catalytic performance of a single functional component, while the integration of MPc and MPor together into crystalline COFs for bifunctional catalysts was still unexplored. Besides, as one of the most important classes of crystalline COFs, Pc-based COFs possess excellent conductivity, mechanical performance and redox-active properties [34,35]. However, the traditional synthesis of Pc-based COFs based on solvothermal methods will inevitably use toxic organic solvents and catalysts [36–40]. Therefore, it is necessary to develop green and efficient methods to synthesize crystalline Pc-based COFs (Scheme 1). Unterlass *et al.* demonstrated that highly crystalline all-aromatic polyimides can be synthesized by hydrothermal polymerization using only H_2O as solvent [41]. Besides, the alcohol-assisted hydrothermal synthesis which was developed by Lotsch *et al.* also confirmed imide-linkage can be obtained without a toxic solvent [42]. On the basis of the above research results, we successfully get a series of crystalline Pc-based COFs. It is noted that our report is the first synthesis of highly crystalline Pc-based COFs by hydrothermal synthesis in pure water without using catalyst and toxic solvents, which conforms to green synthesis chemistry. According to the above H_2O-phase synthesis method, we rationally prepared crystalline NiPc-2HPor COF by condensing a phthalic acid group of NiPc and aromatic amine group of 2HPor through hydrothermal methods (Scheme 1), and further synthesized NiPc-NiPor COF by post-synthesis coordination reaction. The polyimides-linked COFs (PI-COFs) which were formed showed high chemical stability and activity for electrocatalysis MOR coupled with ECR. The porous NiPc-NiPor COF structure not only plays the role of metal site supports, but also possesses high conductivity and regularity. Besides, the Ni in the pockets of MPc and MPor with different chemical environments can act as synergy active sites, thus greatly enhancing ECR coupling MOR catalytic performance.

Above all, the synthesized NiPc-MPor COFs combining the features of crystallinity and conductivity, also have multiple active sites with different chemical environments for ECR and MOR. Among them, the NiPc-NiPor COF shows excellent activity for cathodic ECR (FE_{CO} = 98.12%, j_{CO} = 6.14 mA cm^{-2}) coupled with anodic MOR to HCOOH (FE_{HCOOH} = 93.75%, j_{HCOOH} = 5.81 mA cm^{-2}) in a H-cell at low cell voltage (2.1 V) and exhibits remarkable long-term stability, which is comparable to most reported ECR-MOR coupled catalysts. The *in-situ* Fourier transform infrared spectroscopy (FT-IR) was used to identify the key intermediates for both ECR and MOR. Furthermore, the density functional theory (DFT) calculations demonstrate that the ECR process mainly performs on NiPc unit with the assistance of NiPor, meanwhile, the MOR process shows a preference for NiPor and conjugates with NiPc. The synergistic catalytic effect of NiPc and NiPor combined contributes to such high catalytic activity. This is the first report of bifunctional MPc-MPor-based COFs for electrocatalytic cathodic ECR coupled with anodic MOR simultaneously, which is also of great significance in the field of bifunctional electrocatalysts.

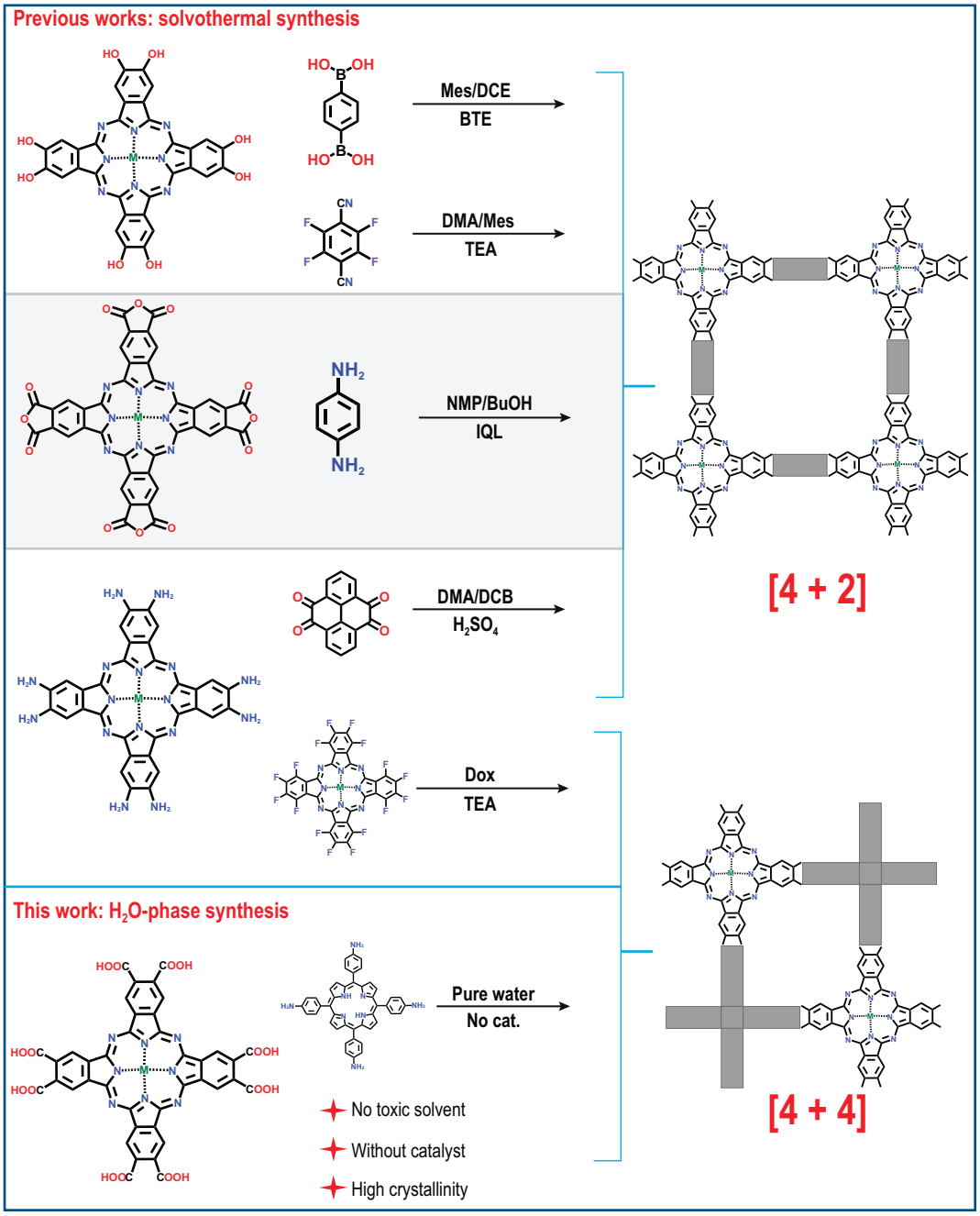

Scheme 1. Schematic representation of design and synthesis of Pc-based COFs. This work and previous works. (Mesitylene (Mes), 1,2-dichloroethane (DCE), Boron trifluoride etherate (BTE), N, N-Dimethylacetamide (DMA), Triethylamine (TEA), N-methylpyrrolidone (NMP), 1-butanol (BuOH), Isoquinoline (IQL), 1,2-dichlorobenzene (DCB), Sulfuric acid (H_2SO_4), 1,4-Dioxane (Dox)).

RESULTS AND DISCUSSION

Synthesis and structure of NiPc-MPor COF

As shown in Scheme 1 and Fig. 1, a [4 + 4] condensation reaction is applied to synthesize NiPc-2HPor COF. Specifically, NiPc-2HPor COF was synthesized by condensation between 2,3,9,10,16,17,23,24-octacarboxyphthalocyanine nickel (NiPc) and 5,10,15,20-tetrakis(para-aminophenyl) porphyrin (2HPor) via hydrothermal methods (Fig. 1a). The crystal structure of NiPc-2HPor COF was characterized by powder X-ray diffraction (PXRD) measurements combined with structural simulation. The AA and AB stacking structural model was constructed based on reticular chemistry, while the

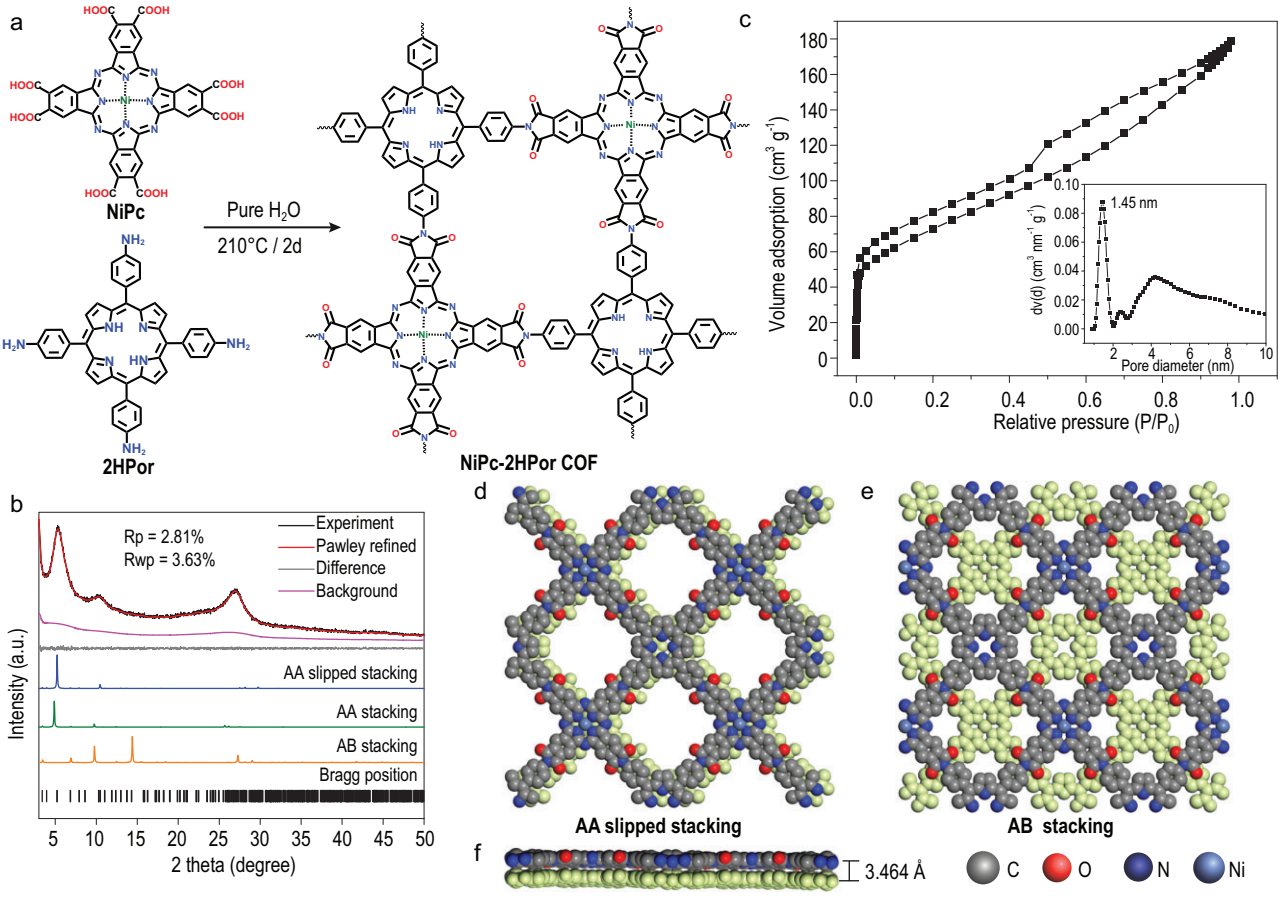

Figure 1. Schematic representation of metallophthalocyanine-porphyrin COFs by polyimide linkage. (a) Schematic of the synthesis and structure of NiPc-2HPor COF through the condensation of NiPc and 2HPor. (b) Simulated and experiment PXRD patterns of NiPc-2HPor COF. (c) N_2 adsorption isotherm of NiPc-2HPor COF. Inset is the pore size distribution. (d) Crystal structure of simulated AA slipped stacking and (e) AB stacking for NiPc-2HPor COF. (f) Side view of AA slipped stacking mode for NiPc-2HPor COF.

results showed that the theoretical PXRD patterns of AA and AB model had some deviations from the experimental curves (Fig. 1b). Interestingly, we found that the theoretical PXRD pattern of AA slipped stacking with *Pm* (6) space group model fitted well with the experimental one (for details, see the structural modeling section). Therefore, we then conducted Pawley refinement based on AA slipped stacking against the experimental PXRD pattern, which provided unit cell parameters of a = b = 25.7859 Å, c = 3.4637 Å, $\alpha = \gamma = 90°$, $\beta = 120°$. The refinement of PXRD diffraction patterns fitted well with the experimental results, with residuals of Rp = 2.81% and Rwp = 3.63%, thus confirming the accuracy of the simulated structure. The peaks at 5.27° and 10.54° are assigned to the (110) and (220) planes, respectively. The porosity of NiPc-2HPor COF was then determined by N_2 adsorption isotherms at 77 K, and the results showed that the pore size distributed at 1.45 nm, which was consistent with the theoretical aperture (Fig. 1c–f). The BET surface area of NiPc-2HPor COF was calculated to be 258.608 $m^2 g^{-1}$. Based on the NiPc-2HPor COF, we further synthesized NiPc-NiPor COF by post-synthesis coordination reaction (Scheme S2). The synthesized NiPc-NiPor COF also shows high crystallinity as confirmed by the PXRD pattern (Fig. 2a). The comparison of PXRD patterns of NiPc-2HPor COF and NiPc-NiPor COF with 2HPor and NiPc show no precursor monomers exist, suggesting the completeness of the polymerization reaction (Fig. S1). Fourier transform infrared (FT-IR) was then conducted to characterize the chemical structure which confirmed the imide formation reaction in NiPc-2HPor COF and NiPc-NiPor COF. As shown in Fig. 2b, the obvious peaks at 1762 and 1707 cm^{-1} correspond to asymmetric and symmetric vibrations of C=O of the five-membered imide rings and the peaks at 1368 and 1324 cm^{-1} belong to the stretching vibration of the C-N-C bond of polyimide [43]. Furthermore, the peaks corresponding to the carboxylic acid of the

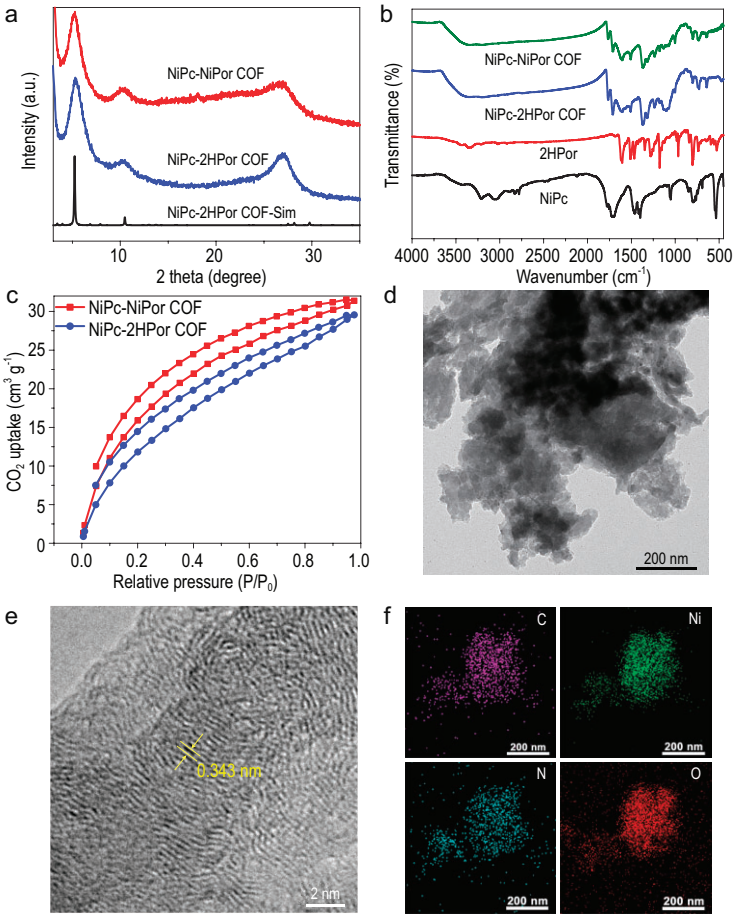

Figure 2. Characterization of NiPc-MPor COFs. (a) The PXRD curve of NiPc-MPor COFs. (b) FT-IR of NiPc-MPor COFs. (c) CO_2 adsorption-desorption isotherms of NiPc-MPor COFs. (d) TEM image of NiPc-NiPor COF. (e) HRTEM image of NiPc-NiPor COF. (f) Element mapping of NiPc-NiPor COF.

precursor NiPc at 1696 cm^{-1} and the amide bond of the NiPor at 1674 cm^{-1} are not observed, which indicates full imidization yielding the desired PI-COFs (Fig. 2b). The thermostability of COFs was studied by thermogravimetric analysis (TGA) under N_2 and O_2 atmosphere (Figs S2–S5), which showed no obvious change up to ∼300°C under both nitrogen and oxygen atmospheres. X-ray photoelectron spectroscopy (XPS) was conducted to confirm all the element states over COFs (Figs S6–S10), which showed C, N, O and Ni coexisting in NiPc-2HPor COF and NiPc-NiPor COF. Furthermore, the analysis results show the divalent state of the central Ni in COFs. We then performed high-resolution XPS and their deconvolution for C1s, N1s and O1s. In the high-resolution N1s spectrum of NiPc-2HPor COF (Fig. S10a), the binding energy peaks at 398.8, 399.2, 399.8 and 400.5 eV corresponding to iminic N, C = N, pyrrolic N and C-N, respectively. As a result, the disappearance of the pyrrolic N peak in NiPc-NiPor COF (Fig. S10d and Table S1) shows the successful post-metalation of Ni [44].

All above results illustrate the successful condensation of NiPc and 2HPor and the formation of PI-COFs. We then performed the CO_2 adsorption-desorption test of these COFs. As shown in Fig. 2c, NiPc-NiPor COF have a strong CO_2 adsorption capacity of about 31.19 $cm^3\ g^{-1}$ in 273 K, which is higher than the NiPc-2HPor COF, and thus is more beneficial for the ECR reaction. The crystal morphology of these COFs was observed by transmission electron microscopy (TEM) and scanning electron microscopy (SEM). The TEM shows that NiPc-NiPor/2HPor COF displays a lamellar shape crystal with a size of ∼50–100 nm (Fig. 2d and Fig. S11). The SEM images of COFs further confirm the microcrystal morphology (Figs S12 and S13). Furthermore, the high-resolution TEM (HRTEM) of NiPc-NiPor COF displays clear lattice fringes of (001) crystal face with a distance of 0.343 nm, which fits well with the theoretical layer distance (0.346 nm), further confirming the precise nature of the simulated crystal structure (Figs 1f and 2e). Energy dispersive X-ray spectroscopy (EDX) mapping reveals the uniform distribution of the Ni, C, N and O element of NiPc-NiPor COF, which illustrates the homogeneity of these materials (Fig. 2f).

Electrocatalytic ECR coupling MOR performance

Based on the above analysis and characterization of the structure and features of NiPc-NiPor COFs, it can be concluded that the MPc and MPor monomers in crystalline COFs form the well-defined, isolated, and atomically uniformly multiple single-metal active sites with different chemical environments, which is favorable for catalytic reaction. The electronic conductivity of NiPc-2HPor COF and NiPc-NiPor COF were performed by current (I)-voltage (V) measurements and electrochemical impedance spectrum (EIS) (Figs S14 and S15). We then calculated the conductivity values of all tested COFs from I-V test results by using a double probe system. As a result, the NiPc-NiPor COF exhibits higher specific conductivity values (7.28E-8 S m^{-1}) than NiPc-2HPor COF (2.5E-8 S m^{-1}). It can be concluded that the NiPc-NiPor COF possesses a superior electron transfer rate, which is due to their highly conjugated π-electron structure. Accordingly, NiPc-NiPor COF will be a more promising platform for electrocatalysis. Bearing the above ideas in mind, we then studied the ECR coupling MOR performances of NiPc-MPor COFs. The separated electrocatalysis tests were first conducted in a

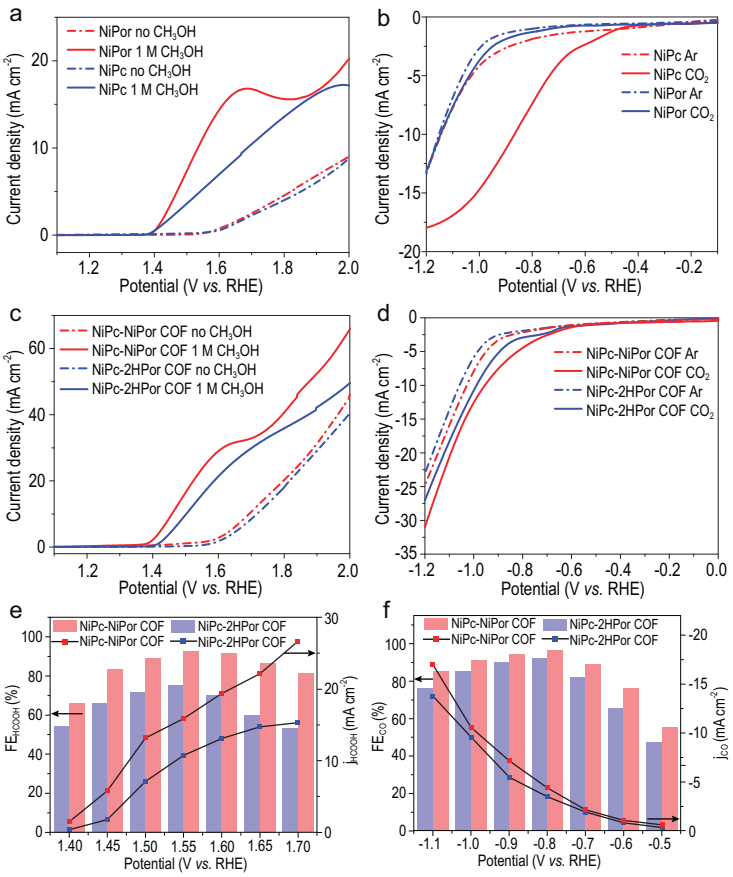

Figure 3. Electrocatalytic CO_2 reduction and CH_3OH oxidation performances of NiPc-MPor COFs. (a) LSV curves of NiPc and NiPor monomer for MOR. (b) LSV curves of NiPc and NiPor monomer for ECR. (c) LSV curves of NiPc-MPor COFs for MOR. (d) LSV curve of NiPc-MPor COFs for ECR. (e) FE and partial current density of NiPc-MPor COFs for MOR. (f) FE and partial current density of NiPc-MPor COFs for ECR.

common H-cell reactor with a three-electrode standard system and the coupling reaction was then performed in the two-electrode system by electrochemical workstation. CO and HCOOH were detected as main the products for ECR and MOR with a minor by-product H_2, which were quantified by gas chromatography (GC) and ion chromatography (IC) by external standard methods (Figs S16–S18), respectively.

First, we studied the NiPc and NiPor monomers as catalysts for MOR by conducting a linear sweep voltammetry (LSV) test on a three-electrode system in 1 M KOH electrolyte with or without methanol substrates, respectively. Interestingly, both NiPc and NiPor show effective enhanced current density for MOR in methanol electrolyte (Fig. 3a). Besides, NiPor monomers exhibit maximum current density when applied in a methanol electrolyte, suggesting that the NiPor may be a more effective active site for MOR. The LSV performance for ECR of NiPc and NiPor monomers also shows that NiPc has a higher current density than NiPor in CO_2 (Fig. 3b), indicating that NiPc may play a key role in ECR. Based on the above results, it is reasonable to assume that integrating NiPc and NiPor monomers will be greatly beneficial to the ECR coupled with MOR performance.

Based on the above consideration, we then conducted the LSV test for NiPc-MPor COFs (Fig. 3). The results show that both NiPc-2HPor COF and NiPc-NiPor COF represent higher current density in methanol electrolyte compared with pure KOH electrolyte along with the increase in applied voltage (Fig. 3c and Fig. S19). Further, NiPc-NiPor COF shows more enhanced current intensity compared to NiPc-2HPor COF, which also indicates that the NiPor in the COF might play a key role in contributing to the activity of MOR. Besides, the Tafel slope of NiPc-NiPor COF at the anode in 1 M KOH with 1 M methanol is 123.84 mV dec^{-1}, much lower than that in the pure KOH electrolyte (318.55 mV dec^{-1}), suggesting that it has more favorable reaction kinetics for MOR (Fig. S20). We then tested the ECR performance for NiPc-MPor COFs as a cathode in Ar and CO_2 saturated solution. Both the NiPc-NiPor COF and NiPc-2HPor COF obtain enhanced current density in the existence of CO_2 compared to Ar environment, which suggests that the ECR is priority to HER process. Furthermore, the current density of NiPc-NiPor COF is almost same as that of NiPc-2HPor COF in a CO_2 environment (Fig. 3d), which further illustrates that the NiPc (rather than NiPor) in COFs mainly contribute to ECR activity.

Encouraged by the above performance, we then explored, separately, the Faradaic efficiency (FE) and partial current density (j) of these samples for ECR or MOR on a three-electrode system in greater detail. We first discovered the NiPc and NiPor monomers under wide potentials ranging from −0.5 V to −1.1 V vs. RHE for cathode ECR and 1.4 V to 1.7 V vs. RHE for anode MOR and calculated the corresponding FE values (Figs S21 and S22). The results show that, for MOR, both the NiPc and NiPor monomers own effective FE_{HCOOH} and the detailed comparison suggests that the NiPor monomer has superior selectivity to NiPc. At the same time, based on the ECR performance as shown in Fig. S22, we can also conclude that the NiPc shows more superior selectivity for ECR. We then studied the NiPc-2HPor COF and NiPc-NiPor COF as catalysts for ECR and MOR tests, separately (Fig. 3e and f). Compared with NiPc-2HPor COF, NiPc-NiPor COF exhibits superior MOR catalytic activity and selectivity with maximal FE_{HCOOH} of up to 92.63% with a j_{HCOOH} of 15.84 mA cm^{-2} at 1.55 V vs. RHE. On the other hand, the NiPc-NiPor COF also shows the better activity than NiPc-2HPor COF on ECR,

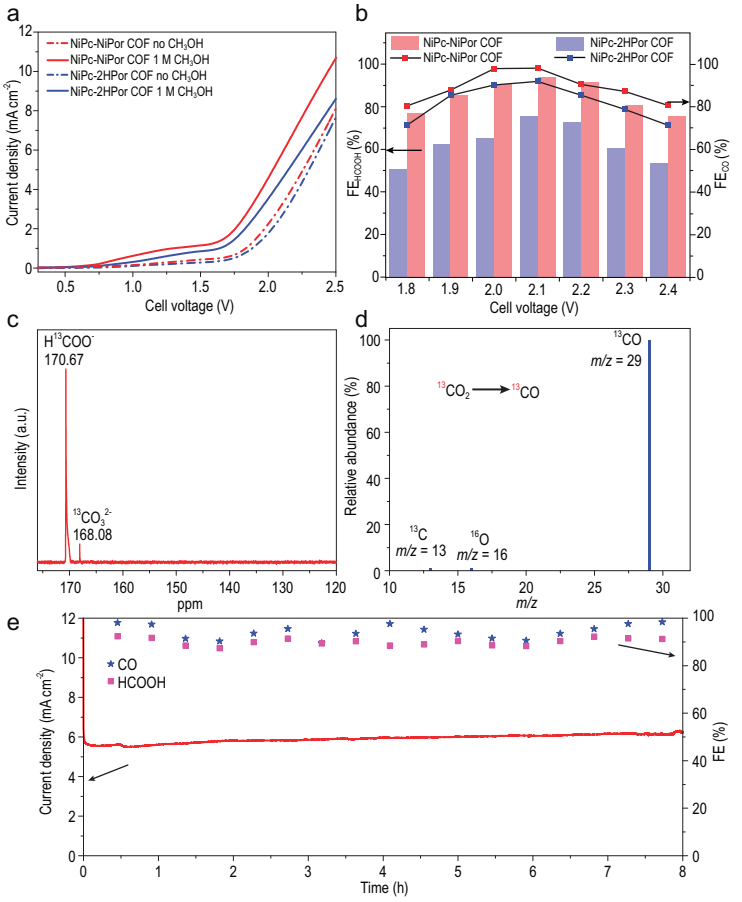

Figure 4. ECR and MOR coupling reaction performance for NiPc-MPor COFs. (a) LSV curves for the coupled ECR || MOR cell for NiPc-MPor COFs. (b) FE performances for the coupled ECR || MOR cell for NiPc-MPor COFs. (c) ^{13}C-NMR spectra of the MOR electrolyte for NiPc-NiPor COF. (d) MS spectra of the ECR to CO for NiPc-NiPor COF. (e) Durability measurements of NiPc-NiPor COF at 2.1 V cell voltage.

with maximal FE_{CO} of up to 96.57% and a partial current density (j_{CO}) of −4.39 mA cm^{-2} at −0.8 V vs. RHE.

Based on the above results, ECR and MOR coupling reaction performances were carried out by using a two-electrode H-cell, in which the NiPc-MPor COFs act as both cathode and anode active catalyst. Specifically, the anode part with 1 mg cm^{-2} NiPc-MPor COFs active layer was applied in 1 M KOH electrolyte containing 1 M methanol, and the cathode with the same active material was applied in 0.5 M $KHCO_3$ electrolyte (denoted as NiPc-MPor COFs || NiPc-MPor COFs). The LSV patterns for the paired MOR (1 M methanol) || ECR show that the NiPc-NiPor COF electrode only needs a cell voltage of 1.5 V to obtain a current density of 1.0 mA cm^{-2}, which is much lower than the paired OER || ECR without methanol (Fig. 4a). We then tested the FE of two COFs under cell voltage ranging from 1.8 V to 2.4 V. When paired the MOR and ECR, the FE_{CO} of NiPc-NiPor COF exhibited higher than 90% in a potential range from 2.0 to 2.2 V and the maximum FE_{CO} can reach up to 98.12% with a partial current density (j_{CO}) of ∼6.14 mA cm^{-2} at 2.1 V (Fig. 4b, and Figs S23 and S25). Meanwhile, NiPc-2HPor COF shows a little less FE_{CO} than the NiPc-NiPor COF for ECR, which can be concluded that the NiPc unit mainly contributed to ECR activity. On the other hand, NiPc-2HPor COF also shows much lower FE_{HCOOH} than NiPc-NiPor COF for MOR, which illustrates that the NiPor may play a key role for MOR. Besides, the corresponding anodic MOR produced HCOOH with FE over 75% at all applied voltages and toward a maximum value of 93.75% with a partial current density (j_{HCOOH}) of ∼5.81 mA cm^{-2} at 2.1 V (Fig. 4b and Fig. S24). The detailed structure-functional relationships will be discussed will in the following part. To further detect the liquid product of NiPc-NiPor COF during MOR process in MOR || ECR cell, the reaction mixture was analyzed by ^{1}H-NMR (Fig. S26). The CH_3OH oxidation products, that is, HCOOH is obviously found in 8.27 ppm. For ECR, the ^{1}H-NMR of reaction mixture shows no liquid products (Fig. S27), and no other except for CO and H_2 is detected from GC and IC, which means CO and H_2 are the only products of ECR. To verify the source of carbon atoms in HCOOH, we carried out isotope labeling. The MOR test was carried out in 1 M KOH electrolyte containing ^{13}C labeled CH_3OH, the ^{13}C-NMR showed an evident peak of H^{13}COOH as shown in Fig. 4c. The isotope labeling experiments were also performed to ascertain the carbon sources of ECR products, i.e. CO, ^{13}CO ($m/z = 29$) was finally detected by gas chromatograph-mass spectrometer (GC-MS) (Fig. 4d). These results confirm that the produced HCOOH and CO originated from the reactant CH_3OH and CO_2, respectively, instead of decomposition of the catalyst. The durability of a catalyst is also one of the most important factors in further practice application. Therefore, we then evaluated the stability of NiPc-NiPor COF in the electrochemical conditions by chronoamperometric testing (Fig. 4e). After long-time evaluation, no obvious decay in FE and current density was detected during 8.5 h (the FE of CO and HCOOH was analyzed every 0.5 h). Furthermore, the crystalline structure was preserved from the PXRD patterns of NiPc-NiPor COF after being immersed in 1 M KOH aqueous solution and 0.5 M $KHCO_3$ aqueous solution for 48 h, respectively (Fig. S28). More importantly, the PXRD patterns show that NiPc-NiPor COF still maintains crystallinity after the electrocatalytic reaction (Fig. S29). It is noticed that the PXRD peak intensity after electrocatalytic tests on anode showed reduced. This phenomenon maybe caused by the intrinsic instability of this COF under the combination

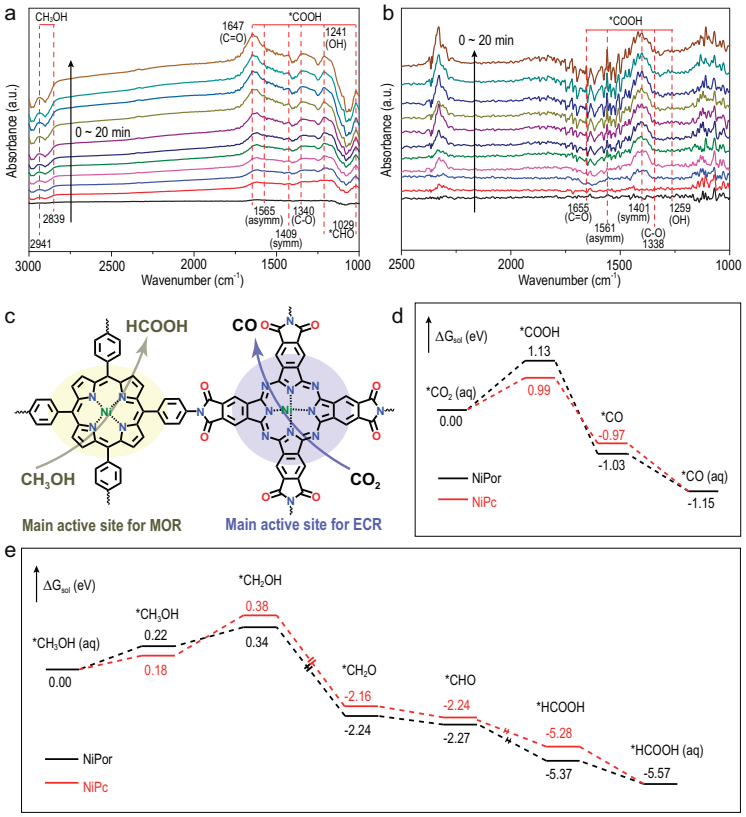

Figure 5. *In-situ* FT-IR and DFT calculations of the catalytic process. (a) *In-situ* FT-IR spectra for MOR using NiPc-NiPor COF as catalyst. (b) *In-situ* FT-IR spectra for ECR using NiPc-NiPor COF as catalyst. (c) Schematic of the mechanism of NiPc-NiPor COF for ECR coupled with MOR. (d) Free energy diagram (FED) of NiPc and NiPor for ECR. (e) FED of NiPc and NiPor for MOR.

of strong base and electric field conditions, the electrochemical corrosion by electrolysis, and mechanical force by stirring. All the above results confirm that these COFs are highly stable catalysts.

Investigating structure-functional relationships

We then performed the *in-situ* FT-IR investigation of the catalytic process to study the key intermediates for ECR and MOR. For the MOR process (Fig. 5a), an increasing positive band centers at ∼1647 cm^{-1} which corresponds to the C=O of *COOH and is clearly observed in applied cell potential of 1.55 V vs. the RHE. Meanwhile, a small positive band centers at 1565, 1409, 1340 and 1241 cm^{-1}, which corresponds to the asymmetry and symmetry stretch of C-O and OH vibrations for *COOH also observed [45]. Besides, the increasing peak at 1029 cm^{-1} suggests that *CHO species exist [46]. The above results show that the *COOH and *CHO are the key intermediates for CH_3OH oxidation to HCOOH. In addition, the bands at 2941 and 2839 cm^{-1} in the spectra are ascribed to surface CH_3OH species. As for the ECR process (Fig. 5b), the *COOH is also observed as a key intermediate for CO_2 reduction to CO, whose peaks appear at 1700–1200 cm^{-1} [47].

Guided by the *in-situ* FT-IR analysis and conclusions, we further investigated the ECR and MOR catalytic processes in detail based on DFT theoretical calculations (Fig. 5c). For the ECR process, the electron transfer to the adsorbed CO_2 was then combined with a H proton to generate *COOH which is calculated to be the rate determining step (RDS) on NiPc-NiPor COF. Interestingly, the Gibbs free energy on NiPc for the RDS step is 0.99 eV, which is obviously smaller than the process on NiPor (Fig. 5d). Therefore, based on the minimum energy principle, the ECR process is more likely to occur on the NiPc part. As for the MOR process, the RDS is determined to be the oxidation process of *CH_3OH to *CH_2OH. It is noted that the energy barrier for *CH_3OH to *CH_2OH on NiPor and NiPc have a small difference, this indicated that the MOR catalytic process can occur in both NiPor and NiPc. From the calculation results, we also found that the free energy for *CH_3OH to *CH_2OH process on NiPor is 0.34 eV, which is slightly weaker compared to NiPc (0.38 eV) (Fig. 5e). Thus, we can conclude that the main active site for MOR contributed to the NiPor part and simultaneously conjugated with NiPc, these synergistic effects caused significant catalytic activity during the MOR reaction.

CONCLUSION

In conclusion, we rationally designed and synthesized two stable PI phthalocyanine-porphyrin bifunctional COFs in pure water by a hydrothermal method for electrocatalytic cathodic CO_2 reduction coupled with anodic CH_3OH oxidation. The dual Ni sites in NiPc-NiPor COF in different chemical environments are mainly devoted to different electrocatalytic reactions (i.e. MOR and ECR). Interestingly, NiPc-NiPor COF behaves as the superior FE and j for both MOR and ECR. In detail, the NiPc-NiPor COF shows FE_{CO} = 98.12% (j_{CO} = 6.14 mA cm^{-2}) for ECR and FE_{HCOOH} = 93.75% (j_{HCOOH} = 5.81 mA cm^{-2}) for MOR. According to exhaustive electrochemical measurement and comparison results, we demonstrate that the NiPc unit mainly contributes to the ECR with the assistance of NiPor, meanwhile NiPor is mainly for the MOR process and conjugates with NiPc. These ingenious synergistic effects cause significant catalytic activity for ECR coupled MOR reaction. More importantly, an in-depth mechanistic study based on *in-situ* FT-IR and DFT simulation also confirmed the above conclusions. Our

work provides a new insight into the design and development of dual functional COFs-based catalysts for various catalytic reactions.

METHODS

Synthesis of PI-linked metallophthalocyanine-metalloporphyrin COFs

Synthesis of NiPc-2HPor COF: A Pyrex tube measuring 10 × 200 mm (o.d × length) was charged with NiPc (23.1 mg), 2HPor (16.8 mg), H_2O (2.5 mL). After sonication for about 60 minutes, the tube was then flash frozen at 77 K (liquid N_2 bath) and degassed by three freeze-pump-thaw cycles, and refilled by N_2 (99.999%) to 1 bar then flame sealed. Then, warmed to room temperature, the mixture was heated at 230°C and left undisturbed for 48 h. A black precipitate was isolated by filtration in a Buchner funnel and was washed with THF and acetone until the filtrate was colorless. The wet sample was transferred to a Soxhlet extractor and washed with THF for 24 hours. Finally, the product was evacuated at 120°C under dynamic vacuum overnight to yield the activated sample (∼21 mg, 57% yield).

Synthesis of NiPc-NiPor COF: The NiPc-NiPor COF was synthesized by post synthesis method. In detail, NiPc-2HPor COF (15 mg) and $Ni(OAc)_2{\cdot}2H_2O$ (50 mg) were added to the ethanol (20 mL). After being purified by N_2, the mixture was heated and refluxed for 12 h at N_2 atmosphere. Following that, the solutions were cooled down to room temperature and filtered. The filter cake was washed thoroughly with water and ethanol to remove free metal ions. The final filter cake was dried at 120°C under dynamic vacuum overnight to get NiPc-NiPor COF (∼14 mg, 82% yield).

Electrochemical measurements

Electrocatalytic ECR coupling MOR experiments: All electrochemical tests were applied in an airtight H-cell (Tianjin Aida Hengsheng Technology, China) which separated the cathodic and anodic chambers by using Nafion 117 membrane. The standard two-electrode system, i.e. catalyst-modified carbon fiber papers both as working anode and cathode electrode, and the ECR coupling MOR tests on the electrochemical workstation (Bio-Logic VSP) and the CO_2 saturated 0.5 M $KHCO_3$ and 1 M CH_3OH in 1 M KOH were used as electrolyte. The potential range of 1.8 to 2.4 V (cell voltage, step size = 0.1 V) was applied during the ECR coupling MOR test and calculated the Faradaic efficiency and current density. The yield of CO and H_2 was quantified by gas chromatography (GC-7920, CEAulight, China). The HCOOH yield was quantified by ion chromatography (Ion Chromatography System, Themorpher, China). The working electrode was similar to the preparation of ECR. The polarization curve results were obtained by performing linear sweep voltammetry (LSV) mode with a scan rate of 5 mV s^{-1}. Potentials were measured against an Ag/AgCl reference electrode and the results were converted to those against a reversible hydrogen electrode (RHE) based on the RHE calibration. Electrochemical impedance spectroscopy (EIS) measurement was performed on the electrochemical analyzer in a frequency range from 100 kHz to 100 mHz by applying an AC voltage with 10 mV.

SUPPLEMENTARY DATA

Supplementary data are available at *NSR* online.

FUNDING

This work was supported by the National Natural Science Foundation of China (22225109, 22071109, 22105080 and 22201083), the Project funded by the China Postdoctoral Science Foundation (2020M682748 and 2021M701270), the Guangdong Basic and Applied Basic Research Foundation (2023A1515010779 and 2023A1515010928), the Guangzhou Basic and Applied Basic Research Fund Project (202102020209) and the China National Postdoctoral Program for Innovative Talents (BX20220115).

AUTHOR CONTRIBUTIONS

Y.-Q. L., and Mi. Z. conceived the idea. J.-P. L. and Mi. Z designed the experiments, collected and analyzed the data. R.-H.L. and other authors assisted with the experiments and characterizations. All authors have approved the final version of the manuscript.

Conflict of interest statement. None declared.

REFERENCES

1. Nitopi S, Bertheussen E, Scott SB *et al.* Progress and perspectives of electrochemical CO_2 reduction on copper in aqueous electrolyte. *Chem Rev* 2019; **119**: 7610–72.
2. Yamazaki Y, Miyaji M, Ishitani O. Utilization of low-concentration CO_2 with molecular catalysts assisted by CO_2-capturing ability of catalysts, additives, or reaction media. *J Am Chem Soc* 2022; **144**: 6640–60.
3. Huang Q, Liu J, Feng L *et al.* Multielectron transportation of polyoxometalate-grafted metalloporphyrin coordination frameworks for selective CO_2-to-CH_4 photoconversion. *Natl Sci Rev* 2020; **7**: 53–63.
4. Birdja YY, Pérez-Gallent E, Figueiredo MC *et al.* Advances and challenges in understanding the electrocatalytic conversion of carbon dioxide to fuels. *Nat Energy* 2019; **4**: 732–45.

5. Ling L-L, Jiao L, Liu X *et al.* Potassium-assisted fabrication of intrinsic defects in porous carbons for electrocatalytic CO_2 reduction. *Adv Mater* 2022; **34**: 2205933.
6. Ma W, Xie S, Liu T *et al.* Electrocatalytic reduction of CO_2 to ethylene and ethanol through hydrogen-assisted C-C coupling over fluorine-modified copper. *Nat Catal* 2020; **3**: 478–87.
7. Nam D-H, Luna P, Rosas-Hernández De A *et al.* Molecular enhancement of heterogeneous CO_2 reduction. *Nat Mater* 2020; **19**: 266–76.
8. Sun S-N, Li N, Liu J *et al.* Identification of the activity source of CO_2 electroreduction by strategic catalytic site distribution in stable supramolecular structure system. *Natl Sci Rev* 2021; **8**: nwaa195.
9. Wang J, Li X, Wang M *et al.* Electrocatalytic valorization of poly(ethylene terephthalate) plastic and CO_2 for simultaneous production of formic acid. *ACS Catal* 2022; **12**: 6722–8.
10. Li R, Xiang K, Peng Z *et al.* Recent advances on electrolysis for simultaneous generation of valuable chemicals at both anode and cathode. *Adv Energy Mater* 2021; **11**: 2102292.
11. Liu W, Bai P, Wei S *et al.* Gadolinium changes the local electron densities of nickel 3d orbitals for efficient electrocatalytic CO_2 reduction. *Angew Chem Int Ed* 2022; **61**: e202201166.
12. Ma W, He X, Wang W *et al.* Electrocatalytic reduction of CO_2 and CO to multicarbon compounds over Cu-based catalysts. *Chem Soc Rev* 2021; **50**: 12897–914.
13. Lai W, Qiao Y, Zhang J *et al.* Design strategies for markedly enhancing energy efficiency in the electrocatalytic CO_2 reduction reaction. *Energy Environ Sci* 2022; **15**: 3603–29.
14. Vass Á, Kormányos A, Kószó Z *et al.* Anode catalysts in CO_2 electrolysis: challenges and untapped opportunities. *ACS Catal* 2022; **12**: 1037–51.
15. Wang T, Tao L, Zhu X *et al.* Combined anodic and cathodic hydrogen production from aldehyde oxidation and hydrogen evolution reaction. *Nat Catal* 2022; **5**: 66–73.
16. Wei X, Li Y, Chen L *et al.* Formic acid electro-synthesis by concurrent cathodic CO_2 reduction and anodic CH_3OH oxidation. *Angew Chem Int Ed* 2021; **60**: 3148–55.
17. Wang Y, Gonell S, Mathiyazhagan UR *et al.* Simultaneous electrosynthesis of syngas and an aldehyde from CO_2 and an alcohol by molecular electrocatalysis. *ACS Appl Energy Mater* 2019; **2**: 97–101.
18. Li T, Cao Y, He J *et al.* Electrolytic CO_2 reduction in tandem with oxidative organic chemistry. *ACS Cent Sci* 2017; **3**: 778–83.
19. Li Y, Huo C-Z, Wang H-J *et al.* Coupling CO_2 reduction with CH_3OH oxidation for efficient electrosynthesis of formate on hierarchical bifunctional CuSn alloy. *Nano Energy* 2022; **98**: 107277.
20. Huang N, Lee KH, Yue Y *et al.* A stable and conductive metallophthalocyanine framework for electrocatalytic carbon dioxide reduction in water. *Angew Chem Int Ed* 2020; **59**: 16587–93.
21. Zhong H, Ghorbani-Asl M, Ly KH *et al.* Synergistic electroreduction of carbon dioxide to carbon monoxide on bimetallic layered conjugated metal-organic frameworks. *Nat Commun* 2020; **11**: 1409.
22. Habib AM, Breedlove BK, Goulven CG *et al.* Enhancement of the electrocatalytic abilities toward CO_2 reduction by tethering redox-active metal complexes to the active site. *Dalton Trans* 2021; **50**: 13368–73.
23. Wu Y, Jiang Z, Lu X *et al.* Domino electroreduction of CO_2 to methanol on a molecular catalyst. *Nature* 2019; **575**: 639–42.
24. Guan X, Fang Q, Yan Y *et al.* Functional regulation and stability engineering of three-dimensional covalent organic frameworks. *Acc Chem Res* 2022; **55**: 1912–27.
25. Zhai Y, Liu G, Jin F *et al.* Construction of covalent-organic frameworks (COFs) from amorphous covalent organic polymers via linkage replacement. *Angew Chem Int Ed* 2019; **58**: 17679–83.
26. Wang X, Chen L, Chong SY *et al.* Sulfone-containing covalent organic frameworks for photocatalytic hydrogen evolution from water. *Nat Chem* 2018; **10**: 1180–9.
27. Yusran Y, Guan X, Li H *et al.* Postsynthetic functionalization of covalent organic frameworks. *Natl Sci Rev* 2020; **7**: 170–90.
28. Zhang M, Chang J-N, Chen Y *et al.* Controllable synthesis of cofs-based multicomponent nanocomposites from core-shell to yolk-shell and hollow-sphere structure for artificial photosynthesis. *Adv Mater* 2021; **33**: 2105002.
29. Lu M, Liu J, Li Q *et al.* Rational design of crystalline covalent organic frameworks for efficient CO_2 photoreduction with H_2O. *Angew Chem Int Ed* 2019; **58**: 12392–7.
30. Li D, Li C, Zhang L *et al.* Metal-free thiophene-sulfur covalent organic frameworks: precise and controllable synthesis of catalytic active sites for oxygen reduction. *J Am Chem Soc* 2020; **142**: 8104–8.
31. Cote AP, Benin AI, Ockwig NW *et al.* Porous, crystalline, covalent organic frameworks. *Science* 2005; **310**: 1166–70.
32. Wang D-G, Qiu T, Guo W *et al.* Covalent organic framework-based materials for energy applications. *Energy Environ Sci* 2021; **14**: 688–728.
33. Ji W, Wang T-X, Ding X *et al.* Porphyrin-and phthalocyanine-based porous organic polymers: from synthesis to application. *Coord Chem Rev* 2021; **439**: 213875.
34. Yang C, Jiang K, Zheng Q *et al.* Chemically stable polyarylether-based metallophthalocyanine frameworks with high carrier mobilities for capacitive energy storage. *J Am Chem Soc* 2021; **143**: 17701–7.
35. Yue Y, Cai P, Xu X *et al.* Conductive metallophthalocyanine framework films with high carrier mobility as efficient chemiresistors. *Angew Chem Int Ed* 2021; **60**: 10806–13.
36. Meng Z, Stolz RM, Mirica KA. Two-dimensional chemiresistive covalent organic framework with high intrinsic conductivity. *J Am Chem Soc* 2019; **141**: 11929–37.
37. Yue Y, Li H, Chen H *et al.* Piperazine-linked covalent organic frameworks with high electrical conductivity. *J Am Chem Soc* 2022; **144**: 2873–8.
38. Han B, Ding X, Yu B *et al.* Two-dimensional covalent organic frameworks with cobalt(II)-phthalocyanine sites for efficient electrocatalytic carbon dioxide reduction. *J Am Chem Soc* 2021; **143**: 7104–13.
39. Spitler EL and Dichtel WR. Lewis acid-catalysed formation of two-dimensional phthalocyanine covalent organic frameworks. *Nat Chem* 2010; **2**: 672–7.
40. Lu M, Zhang M, Liu C-G *et al.* Stable dioxin-linked metallophthalocyanine covalent organic frameworks (COFs) as photo-coupled electrocatalysts for CO_2 reduction. *Angew Chem Int Ed* 2021; **60**: 4864–71.
41. Lahnsteiner M, Caldera M, Moura HM *et al.* Hydrothermal polymerization of porous aromatic polyimide networks and machine learning-assisted computational morphology evolution interpretation. *J Mater Chem A* 2021; **9**: 19754–69.
42. Maschita J, Banerjee T, Lotsch BV. Direct and linker-exchange alcohol-assisted hydrothermal synthesis of imide-linked covalent organic frameworks. *Chem Mater* 2022; **34**: 2249–58.
43. Fang Q, Zhuang Z, Gu S *et al.* Designed synthesis of large-pore crystalline polyimide covalent organic frameworks. *Nat Commun* 2014; **5**: 4503.

44. Biswal BP, Valligatla S, Wang M *et al.* Nonlinear optical switching in regioregular porphyrin covalent organic frameworks. *Angew Chem Int Ed* 2019; **58**: 6896–900.
45. Xie W, Li H, Cui G *et al.* NiSn atomic pair on an integrated electrode for synergistic electrocatalytic CO_2 reduction. *Angew Chem Int Ed* 2021; **60**: 7382–8.
46. Qiu X-F, Zhu H-L, Huang J-R *et al.* Highly selective CO_2 electroreduction to C_2H_4 using a metal-organic framework with dual active sites. *J Am Chem Soc* 2021; **143**: 7242–6.
47. Sun S-N, Dong L-Z, Li J-R *et al.* Redox-active crystalline coordination catalyst for hybrid electrocatalytic methanol oxidation and CO_2 reduction. *Angew Chem Int Ed* 2022; **61**: e202207282.